Journal of Materials Chemistry B

ROYAL SOCIETY OF CHEMISTRY

PAPER

View Article Online
View Journal | View Issue

Cite this: J. Mater. Chem. B, 2023, 11, 5544

Poisson–Nernst–Planck framework for modelling ionic strain and temperature sensors

Gaurav Balakrishnan, [a] Jiwoo Song,[a] Aditya S. Khair [b] and Christopher J. Bettinger*[ac]

Received 28th December 2022,
Accepted 17th February 2023

DOI: 10.1039/d2tb02819k

rsc.li/materials-b

Ionically conductive hydrogels are gaining traction as sensing and structural materials for use bioelectronic devices. Hydrogels that feature large mechanical compliances and tractable ionic conductivities are compelling materials that can sense physiological states and potentially modulate the stimulation of excitable tissue because of the congruence in electro-mechanical properties across the tissue-material interface. However, interfacing ionic hydrogels with conventional DC voltage-based circuits poses several technical challenges including electrode delamination, electrochemical reaction, and drifting contact impedance. Utilizing alternating voltages to probe ion-relaxation dynamics has been shown to be a viable alternative for strain and temperature sensing. In this work, we present a Poisson–Nernst–Planck theoretical framework to model ion transport under alternating fields within conductors subject to varying strains and temperatures. Using simulated impedance spectra, we develop key insights about the relationship between frequency of the applied voltage perturbation and sensitivity. Lastly, we perform preliminary experimental characterization to demonstrate the applicability of the proposed theory. We believe this work provides a useful perspective that is applicable to the design of a variety of ionic hydrogel-based sensors for biomedical and soft robotic applications.

10th Anniversary Statement

Happy 10 year Anniversary to the editors, associate editors, staff, and the entire *Journal of Materials Chemistry B* team! JMCB has been a trusted partner in helping the Bettinger group disseminate our discoveries in biomaterials and biomaterials science to the scientific community. We are grateful for the long-term and productive partnership that we have forged together over the years. Our lab looks forward to continuing this collaboration for decades more in the future.

Introduction

Synthetic and natural polymer-based hydrogels are being explored as structural and sensing elements for using in implantable and wearable bioelectronics systems.[1–4] Their similarity in physiochemical properties to soft biological tissue has shown improved biocompatibility and integration with the human body in comparison to other materials.[5–9] As a result, hydrogel-based bioelectronics have been utilized in interfacing with the peripheral nervous system,[10,11] the cardiac system,[12] and the skin.[13,14] Hydrogels have been used as various components in sensors such as structural elements and substrates,[15,16] coatings and intermediate layers,[17,18] and sensing elements.[19,20] Heterogenous integration of the electronics with hydrogels has proved challenging arising from manufacturing incompatibilities between swollen polymer networks and typical microfabrication techniques, including the use of solvents, acids, strong vacuums and high temperatures.[4,21–24] As a result, conductive hydrogels are being explored to serve as the primary device components with common applications thus far including strain and temperature sensing.[25–28]

Strain sensing has several applications in physiological monitoring including cardiac and respiratory output,[12,29,30] pressure and tactile sensing,[31–33] and muscular function.[34,35] Temperature can also be used as a physiological marker of health,[36] internal organ function,[37] and tracking wound healing.[38] For many such applications, fully hydrogel-based sensors promise low biotoxicity,[39,40] high conformity and adhesion with soft curvilinear tissues,[41,42] and integration and consolidation with the biological environment.[43,44]

[a] Materials Science and Engineering, Carnegie Mellon University, 5000 Forbes Avenue, Pittsburgh, PA 15213, USA. E-mail: cbetting@andrew.cmu.edu
[b] Chemical Engineering, Carnegie Mellon University, 5000 Forbes Avenue, Pittsburgh, PA 15213, USA
[c] Biomedical Engineering, Carnegie Mellon University, 5000 Forbes Avenue, Pittsburgh, PA 15213, USA

To replace conventional thin-film metal conductors typically operated under non-alternating DC voltages, there has been a targeted effort in increasing the conductivity of soft hydrogels. This has been pursued through two primary means: (i) using conductive polymers such as PEDOT:PSS to form the hydrogel matrix;[19,45,46] and (ii) utilizing conductive fillers such as metallic nano- and micro-particles (Au, Ag, Pt), carbon-based materials, ionic liquids,[47–49] and MXenes within polymer matrices.[50–54]

There has been considerable success in applying these materials in sensing both mechanical deformation and temperature.[55–58] However, there remain considerable barriers to adopting conductive hydrogels as a replacement to conventional conductors. These include electrochemical and mechanical stability, toxicity and biocompatibility of nanoparticle fillers and conjugated polymers, and the apparent trade-off between mechanical compliance and electrical conductivity.[59–63]

Ionic strain sensing has been explored for wearable devices,[33,64] soft robotics,[22,49] and cardiac output monitoring.[12] Recent work has demonstrated that ionically conductive gels can also be designed to accurately monitor body temperature through wearable devices.[32,65] Utilizing AC voltages and electrochemical impedance has been proposed as alternate measurement technique for hydrogel-based sensors (Fig. 1a).[66–68] Electrochemical impedance spectroscopy (EIS) employs a range of small-amplitude AC voltage frequencies to probe ionic transport and relaxation phenomena in electrolytes.[69] Using equivalent circuit models the electrode–electrolyte interface (Fig. 1b) can be described as a combination of physical parameters such as the double layer capacitance, bulk capacitance between electrodes, and solution resistance. These parameters can be extracted from recorded impedance spectra through data fitting (Fig. 1c).[70,71] This eliminates the need to prioritize electronic conductivity using conjugated polymers and filler materials. Further, this technique is commonly applied in non-faradaic regimes with small voltage amplitudes (~10 mV), contributing to electrochemical stability of the hydrogel conductors. Therefore, it is a non-destructive technique that avoids limitations of DC sensing techniques such as drifting interfacial impedance, electrode delamination, and faradaic reactions.

Here, we develop a theoretical framework to model electrochemical impedance spectra of ionic conductors, specifically in use as strain and temperature sensors. Using the Poisson–Nernst–Planck (PNP) system of equations, we build a microscopic picture of ions under the influence of the alternating electric fields. By varying the length scale and temperature of the electrochemical cell, we model the performance of ionic conductors as strain and temperature sensors, respectively. Further, we perform experimental characterization of strain and temperature sensing using sodium chloride (NaCl) electrolytes.

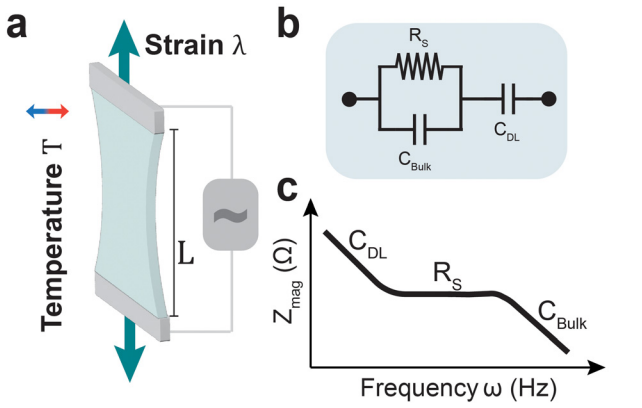

Fig. 1 (a) Schematic of ionic conductor system for strain and temperature sensing. (b) Electrode–electrolyte equivalent circuit model that can be used to represent the ionic conductor. (c) Representative electrochemical impedance spectra labelled with each circuit element comprising the equivalent circuit model.

Poisson–Nernst–Planck model

The Poisson–Nernst–Planck (PNP) framework consists of non-linear partial differential equations that model the behaviour of ions under electric fields.[72] Applying oscillatory voltage fields within PNP equations allow for the modelling of electrochemical impedance properties of ionic systems.[73–75] This approach has been successfully used to model the impedance of a variety of aqueous electrolytes and ionically conductive hydrogel systems.

In this work, we model the electrochemical cell as a 1-dimensional system with an electrolyte sandwiched between ideally polarizable parallel-plate electrodes (Fig. 2). The Poisson equation (eqn (1)) describes a relationship between spatial charge distribution and a changing electric field. The Nernst–Planck equation (eqn (2)) encodes the nature of ion transport arising from a combination of passive diffusion and electromigration.

$$\varepsilon\frac{\partial^2\phi}{\partial x^2} = -e(z_+n_+ + z_-n_-) \tag{1}$$

Here ε, ϕ, e, $z_{+,-}$, and $n_{+,-}$ refer to the dielectric permittivity, potential, charge of a proton, charge of each ion (positive for cation and negative for anion), and concentration of each ion respectively.

$$\frac{\partial n_i}{\partial t} = \frac{\partial j_i}{\partial x} = D_i\left[\frac{\partial^2 n_i}{\partial x^2} + \frac{z_i e}{k_B T}\frac{\partial}{\partial x}\left(n_i\frac{\partial\phi}{\partial x}\right)\right] \tag{2}$$

Here i indexes the positive and negative ions. Additionally, j, D, k_B, and T refer to the ionic flux, individual ionic diffusion

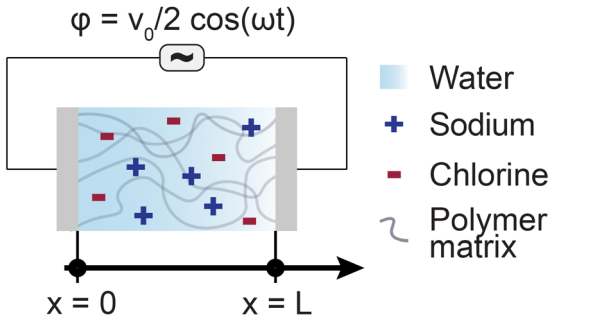

Fig. 2 Schematic of electrochemical cell used in defining the Poisson–Nernst–Planck problem set-up.

coefficient, the Boltzmann constant, and temperature respectively.

We also apply appropriate boundary conditions at each electrode to further define the problem. The first set of boundary conditions (eqn (3)) arises from the oscillating potential applied at each electrode ($x = 0$ and $x = L$).

$$\phi = \pm\frac{v_0}{2}\cos(\omega t) \tag{3}$$

Here v_0, ω and t refer to the amplitude of the applied voltage perturbation, frequency of the voltage waveform and time respectively. The second set of boundary conditions (eqn (4)) is a result of defining zero ionic flux across each electrode.

$$\frac{\partial n_i}{\partial x} = -z_i n_i \frac{\partial \phi}{\partial x} \tag{4}$$

Here z refers to the charge on each ion.

We non-dimensionalize the system of equations using normalization parameters in Table 1 followed by linearization using perturbation expansions for ion density and potential (eqn (5) and (6)). For convenience, we switch from using trigonometric functions to complex exponentials to define the oscillatory perturbations.

$$\tilde{n}_i = \tilde{n}_0 + \tilde{n}_{i,1}e^{i\omega t} \tag{5}$$

$$\tilde{\phi} = \tilde{\phi}_1 e^{i\omega t} \tag{6}$$

By expanding the normalized PNP equations and neglecting terms that are quadratic in the voltage amplitude, we arrive at a system of non-dimensional linear ordinary differential equations (ODEs; eqn (7) and (8)). This simplification is appropriate for the small voltage amplitudes for which the current response is linear.

$$\frac{\partial^2 \tilde{\phi}}{\partial \tilde{x}^2} = -\frac{e^2 n_0 L^2}{k_B T \varepsilon}(z_+\tilde{n}_+ + z_-\tilde{n}_-) \tag{7}$$

$$\frac{\partial \tilde{n}_i}{\partial \tilde{t}} = \frac{\tau_{RC} D_i}{L^2}\left[\frac{\partial^2 \tilde{n}_i}{\partial \tilde{x}^2} + z_i \frac{\partial}{\partial \tilde{x}}\left(\tilde{n}_i \frac{\partial \tilde{\phi}}{\partial \tilde{x}}\right)\right] \tag{8}$$

and boundary conditions (eqn (9) and (10)).

$$\pm\tilde{\phi}_1 = \frac{v_0}{2} \tag{9}$$

$$\frac{\partial \tilde{n}_i}{\partial \tilde{x}} = -z_i \tilde{n}_{i,0} \frac{\partial \tilde{\phi}_i}{\partial \tilde{x}} \tag{10}$$

With the presented problem set-up and parameters defined in Table 2, we utilized a boundary value problem solver on MATLAB (bvp4c) to solve the system of ODEs over the range of intended oscillation frequencies. The impedance is calculated by using the solution of the electric potential to find the ratio of the change in voltage and produced current at the electrode surface (eqn (11)).

$$Z = \frac{V_0}{\varepsilon S i\omega \frac{d\phi_1}{dx}} \tag{11}$$

Here, S is referring to the surface area of the electrode. From eqn (11), the impedance calculated is a complex number with the real and imaginary components arising from the resistive and capacitive elements of the system respectively.

To apply this model for evaluating ionic strain and temperature sensors, we vary the distance between the electrodes L and temperature T, respectively.

Currently, the theoretical framework assumes small ion mobility within the aqueous electrolyte as the dominant contributor to the hydrogel's electrochemical properties. This can serve as an accurate representation for ideally crosslinked polymer networks without significant polymer segment mobility. However, in realistic non-ideal polymer networks, there is a possibility of polymer segment motion contributing to the overall electrochemical nature of the system. While these effects are highly system dependent, their contributions can add to the Nernst–Planck equation (eqn (2)) as additional flux terms.

Table 1 Definitions of normalization term to non-dimensionalize the PNP equations

Parameter	Normalization term	Non-dimensional variable
Ionic density n_i	Bulk ionic density n_0	$\tilde{n}_i = n_i/n_0$
Voltage ϕ (V)	Thermal voltage $\phi_0 = k_B T/e$	$\tilde{\phi} = \phi/\phi_0$
Spatial dimension x (m)	Electrode spacing L	$\tilde{x} = x/L$
Time t (s)	RC time constant τ_{RC}	$\tilde{t} = t/\tau_{RC}$

Results and discussion

Theoretical strain sensing performance

The PNP framework was applied to understand the performance of ionic conductors in measuring strain. The primary variable between simulation groups is the distance between the parallel plate electrodes (L). The magnitude of impedance increases with increasing strain, particularly in the mid-to-high frequency regimes (Fig. 3a).

Further, the real and imaginary components of impedance are plotted *versus* frequency to highlight their intersection. The frequency of intersection indicates the inverse of time constant related to solution resistance and bulk capacitance RC-circuit (Fig. 3b(i)). We find this time constant remains the same for all applied strains. This arises from the change in cell length L has opposing effects on the resistance ($R_S = \rho L/S$) and capacitance ($C_{Bulk} = S\varepsilon/L$). This is further illustrated by fitting the data using the equivalent circuit model presented in Fig. 1b.

There is linear increase and decrease in the solution resistance and bulk capacitance respectively (Fig. 3b(ii)). Further, the average time constant calculated by multiplying the two is 5.64×10^{-10} s, with a highly tight distribution (s.d. 5.99×10^{-13} s).

During practical applications of impedance-based strain sensors, there is often a single frequency at which measurements are acquired. Using the PNP simulations, we provide insight on the relationship between strain sensitivity and measurement frequency (Fig. 3c).

The strain sensitivity is denoted by gauge factor, the ratio between the normalized change in impedance and applied strain (eqn (12)).

Table 2 Definitions of parameters used in the PNP model

Voltage v_0 = 10 mV	Bulk ionic density n_0 = 0.1 M
Sodium diffusivity D_{Na} = 1.33 × 10^{-9} m^2 s^{-1}	Chlorine diffusivity D_{Cl} = 2.03 × 10^{-9} m^2 s^{-1}
Sodium charge z_{Na} = +1	Chlorine charge z_{Cl} = −1
Channel width L = 10 μm	Electrode area S = 1 mm^2
Temperature T = 297 K	Relative permittivity of water ε_{water} = 80.4

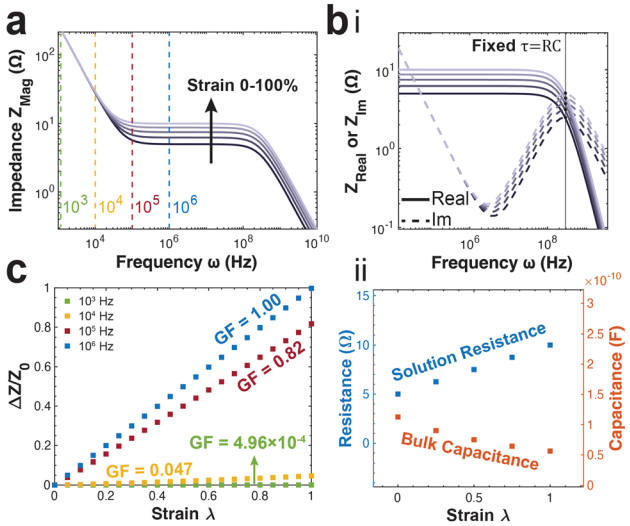

Fig. 3 Theoretical evaluation of ionic conductors as impedance-based strain sensors. (a) Impedance magnitude *versus* frequency plotted for varying strains (0, 25, 50, 75 and 100% – dark to light). The green, yellow, red and blue dotted lines indicate specific frequencies at which strain sensitivity is measured. (b) (i) Mid-to-high frequency regime of the impedance spectra plotted with real and imaginary components separately. The intersection of the real and imaginary plots denotes the frequency related to the inverse of the RC-time constant. (ii) Solution resistance and bulk capacitance values plotted *versus* strain. (c) Strain sensitivity analysis at 10^3 (green), 10^4 (yellow), 10^5 (red) and 10^6 Hz (blue).

$$\mathrm{GF} = \frac{\Delta Z}{Z_0 \lambda} \tag{12}$$

We find that the sensitivity of ionic conductors to strain, denoted by the gauge factor, is highly compromised at lower frequencies. For instance, at 1000 Hz the gauge factor is as low as 4.96 × 10^{-4}. The gauge factor for the ionic strain sensors approaches 1 as frequencies approach the resistive regime of the ionic conductor. The gauge factor is maintained at higher frequencies corresponding to the bulk capacitive regime as its impedance also scales linearly with length scale. Note that using the simplified 1-D electrochemical cell coupled with a purely electrochemical theoretical framework, we have an upper bound for the gauge factor of 1. This is a result of assuming no change in cross-sectional area, therefore the only determinant of impedance change is the length-scale.

Theoretical temperature sensing performance

The PNP framework was applied to evaluate the performance of ionic conductors as temperature sensors. With biological application in mind, we investigated variations in temperature between room temperature and 40 °C.

By varying temperature in the PNP framework, we are modulating the diffusion coefficients of the ions *via* the Stokes–Einstein relationship (eqn (13)) and the Debye length (eqn (14)).

$$D = \frac{k_B T}{6\pi\eta(T)R} \tag{13}$$

$$\lambda_D = \left(\frac{k_B T \varepsilon_{comp}}{\sum_i n_i (z_i e)^2} \right)^{1/2}. \tag{14}$$

Here, η is the temperature-dependent viscosity of water and R is radius of the ion.

With increasing ionic diffusion coefficients, we expect a decrease in impedance with increasing temperature particularly in the resistive frequency regime. This is reflected in the predicted spectra, with the greatest difference between spectra reflected specifically in the resistive regime (Fig. 4a). Unlike the group with varying strain, the intersection of the real and imaginary impedances in the high frequency regime do not fall at the same frequency (Fig. 4b(i)). This indicates a changing time constant for the solution resistance and bulk capacitance RC-circuit. This is further supported examining the equivalent circuit parameters obtained from data fitting. As expected, we observe a decrease in solution resistance with increasing temperature, however the bulk capacitance remains constant with temperature (Fig. 4b(ii)). This is primarily because the bulk capacitance doesn't depend directly on the diffusion coefficient of ions.

Like strain sensing, there is also a need to understand the frequency dependence of impedance-based temperature sensing. Temperature sensitivity (k) is defined as the ratio of normalized impedance change to change in temperature (eqn (15)).

$$k = \frac{\Delta Z}{Z_0 \Delta T} \tag{15}$$

There is greater variation in the trends of temperature sensitivity compared to strain sensitivity with varying sampling frequencies (Fig. 4c). The highest sensitivity is observed only at frequencies where the response is purely resistive (S = −0.034 $°C^{-1}$).

At low frequencies approaching the double layer capacitive regime, we notice a low but positive temperature sensitivity value. This arises from a decrease in double layer capacitance with increasing temperature as a result of an increase in the Debye length. In the high frequency bulk capacitive regime, the temperature sensitivity remains negative but approaches zero. This is a direct result of the varying solution resistance, but fixed bulk capacitance as previously shown.

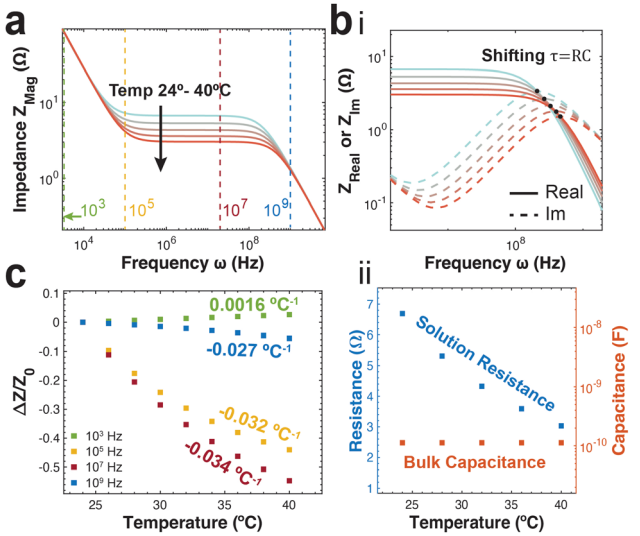

Fig. 4 Theoretical evaluation of ionic conductors as impedance-based temperature sensors. (a) Impedance magnitude *versus* frequency plotted for varying temperatures (24, 28, 32, 36 and 40 °C – blue to red). The green, yellow, red and blue dotted lines indicate specific frequencies at which temperature sensitivity is measured. (b) (i) Mid-to-high frequency regime of the impedance spectra plotted with real and imaginary components separately. The intersection of the real and imaginary plots denotes the frequency related to the inverse of the RC-time constant. (ii) Solution resistance and bulk capacitance values plotted *versus* temperature. (c) Temperature sensitivity analysis at 10^3 (green), 10^4 (yellow), 10^5 (red) and 10^6 Hz (blue).

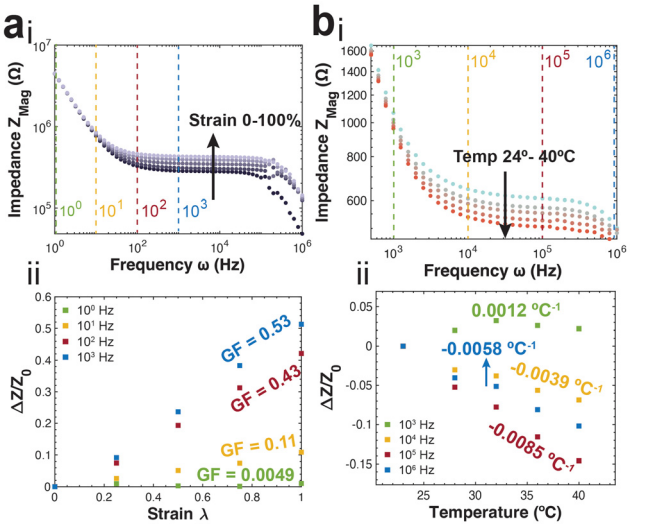

Fig. 5 Experimental evaluation of ionic conductors for strain and temperature sensing. (a) (i) Impedance magnitude *versus* frequency plotted for varying strains (0, 25, 50, 75 and 100% – dark to light). The green, yellow, red and blue dotted lines indicate specific frequencies at which strain sensitivity is measure, (ii) strain sensitivity analysis at 10^0 (green), 10^1 (yellow), 10^2 (red) and 10^3 Hz (blue). (b) (i) Impedance magnitude *versus* frequency plotted for varying temperatures (RT, 28, 32, 36 and 40 °C – blue to red). The green, yellow, red and blue dotted lines indicate specific frequencies at which temperature sensitivity is measured, (ii) temperature sensitivity analysis at 10^3 (green), 10^4 (yellow), 10^5 (red) and 10^6 Hz (blue).

Experimental characterization of strain and temperature sensing

To apply the insight gained from the PNP framework to practical applications, we perform a series of preliminary experiments. First, we utilize gelatin-based ionic hydrogels and measure impedance spectra at specific applied strains. Briefly, glycerol plasticized gelatin networks were infiltrated with 0.1 M NaCl solution. Sections of the gel were placed in custom built tensile manipulators and interfaced with conductive leads. The impedance spectra measured at the varying strains (0, 25, 50, 75, 100%) demonstrate close agreement to the theoretical spectra (Fig. 5a(i)). Specifically, there is an increase in average impedance correlated with increasing strain that begins in the mid-frequency regime corresponding to the resistive region that extends into the high frequency bulk capacitive region. This is further reflected in the strain sensitivity analysis, with the ionic conductors demonstrating increasing sensitivity and gauge factors as we sample from the low-frequency to the mid-frequency regimes (Fig. 5a(ii)). This is a trend that also demonstrates close agreement with the predicted trend.

Next, we also obtain experimental measurements from coplanar microelectrodes in an 0.1 M NaCl solution at varying temperatures (24, 28, 32, 36, 40 °C). The impedance spectra, in agreement with the theory, show a decrease in average impedance with increasing temperature, specifically in the resistive mid-frequency regime (Fig. 5b(i)). At both the high and low frequency regimes, we observe a convergence of the impedance spectra obtained at varying temperatures. An analysis of the temperature sensitivity at varying frequencies shows similar results to the theoretical prediction (Fig. 5b(ii)).

We find that at a low frequency, corresponding to the double layer capacitance there is a positive sensitivity to increasing temperature resulting from an increase to the Debye length. This is in opposition to the higher frequencies, displaying a negative sensitivity indicating a decrease in impedance with increasing temperature as a result of elevated ionic diffusion coefficients. The impedance response to temperature is found to be most sensitive when sampled at frequencies only corresponding to the resistive regime (10^5 Hz; -0.0085 °C^{-1}).

For both strain and temperature sensing, there is a noticeable difference in the frequency regime of interest between the theoretical and experimental results. This is primarily attributed to the differences in the electrochemical cell set-up between theory and experiment. For instance, the cell length used in the theoretical model is significantly smaller than the experimental set-up as a result of computational limitations associated with resolving the sharp variations in ion densities and electric potential near the electrodes. This causes the impedance variation to shift to higher frequencies in the theoretical model, although the trend of impedance variation with frequency measured from experimental data matches well with the theoretical predictions. Further, the theoretical framework simplifies a complex 3-dimensional system of impedance between co-planar electrodes into a 1-dimensional approximation of impedance between parallel electrodes. While there is room to create a more physically accurate theoretical model, this simplified model

provides extremely relevant insights into the trends reflected in the experimental data.

Conclusions

In this work, we present a theoretical framework based on a Poisson–Nernst–Planck framework to model ionic conductors as strain and temperature sensors. By analysing predicted impedance spectra under varying temperature and strains, we present important insights about the relationship of strain and temperature sensitivity and the frequency of the applied voltage perturbation. We utilize experiments to confirm the validity of the theoretical framework and demonstrate their practical application. Specifically, we find that ionic conductors can be sampled at frequency regimes within or higher than the solution resistive domain to achieve the highest capable gauge factor. Temperature sensitivity can be optimized by sampling at frequencies within the solution resistance domain. This work provides important analytical frameworks that can be broadly applied in the design of ionic hydrogel-based sensors for a variety of wearable device and soft robotics applications. Future work in this area can include coupling mechanical modelling with the Poisson–Nernst–Planck framework presented here for predictive sensor optimization and design.

Methods

Synthesis and strain characterization of gelatin hydrogels

Gelatin (10% w/w, 300 bloom type A, Sigma Aldrich) was heated in DI water with 0.1 M NaCl at 65 °C until fully dissolved. The solution was poured into a custom acrylic mold and gelled in ambient conditions for 48 h. Potentiostatic EIS was conducted between 1 and 10^6 Hz with an amplitude of 20 mV (Interface 1000e, Gamry Instruments, Warminster, PA) while the hydrogel strain was controlled using a custom-machined micromanipulator.

Microfabricating thin-film electrodes

Platinum thin-film (100 nm) electrodes were evaporated (Lesker PRO Line PVD75 Electron Beam Evaporator) and photolithographically patterned. The electrodes were encapsulated with Parylene-C (300 nm; SCS Parylene Labcoater 2) and etched using reactive ion etching (50 W, 60 sccm O_2 6 min; Phantom RIE, Trion Tech) to expose electrodes and contacts.

Temperature sensing

Thin-film electrodes (1 mm diameter) were placed in a beaker containing 0.1 M NaCl. The temperature of the solution was controlled by submerging it in an oil bath for even heating. Two-electrode potentiostatic electrochemical impedance spectra were recorded using a GAMRY 1000e potentiostat (Gamry Instruments, PA USA) from 1 to 10^6 Hz over the temperature range of interest (RT to 40 °C).

Author contributions

G. B., A. S. K. and C. J. B. contributed to conceptualization and planning. G. B. and J. S. conducted and implemented the work. G. B. prepared the manuscript draft and all authors provided edits. J. S., A. S. K., and C. J. B. revised the manuscript.

Conflicts of interest

There are no conflicts to declare.

Acknowledgements

The authors acknowledge funding from the following sources: National Institutes of Health Grants R21EB026073 and R21EB028418. GB acknowledges the Carnegie Mellon University Presidential Fellowship and the Carnegie Mellon Ronald F. and Janice A. Zollo Fellowship in Neuroengineering for financial support.

Notes and references

1 H. Yuk, B. Lu and X. Zhao, *Chem. Soc. Rev.*, 2019, **48**, 1642–1667.
2 F. Fu, J. Wang, H. Zeng and J. Yu, *ACS Mater. Lett.*, 2020, **2**, 1287–1301.
3 Y. Liu, T. Yang, Y. Zhang, G. Qu, S. Wei, Z. Liu and T. Kong, *Adv. Mater.*, 2019, **31**, 1902783.
4 G. Balakrishnan, J. Song, C. Mou and C. J. Bettinger, *Adv. Mater.*, 2022, **34**, 2106787.
5 S. Naahidi, M. Jafari, M. Logan, Y. Wang, Y. Yuan, H. Bae, B. Dixon and P. Chen, *Biotechnol. Adv.*, 2017, **35**, 530–544.
6 G. Shi, W. Chen, Y. Zhang, X. Dai, X. Zhang and Z. Wu, *Langmuir*, 2019, **35**, 1837–1845.
7 Y. S. Zhang and A. Khademhosseini, *Science*, 2017, **356**, eaaf3627.
8 E. Caló and V. V. Khutoryanskiy, *Eur. Polym. J.*, 2015, **65**, 252–267.
9 L. Lei, D. Huang, H. Gao, B. He, J. Cao and N. A. Peppas, *Sci. Adv.*, 2022, **8**, eadc8738.
10 W.-C. Huang, X. C. Ong, I. S. Kwon, C. Gopinath, L. E. Fisher, H. Wu, G. K. Fedder, R. A. Gaunt and C. J. Bettinger, *Adv. Funct. Mater.*, 2018, **28**, 1801059.
11 C. C. Horn, M. Forssell, M. Sciullo, J. E. Harms, S. Fulton, C. Mou, F. Sun, T. W. Simpson, G. Xiao, L. E. Fisher, C. Bettinger and G. K. Fedder, *J. Neural Eng.*, 2021, **18**, 055008.
12 J. Song, C. Mou, G. Balakrishnan, Y. Wang, M. Rajagopalan, A. Schreiner, D. Naik, T. Cohen-Karni, M. S. Halbreiner and C. J. Bettinger, *Adv. NanoBiomed Res.*, 2023, **3**, 2200132.
13 C. Lim, Y. J. Hong, J. Jung, Y. Shin, S.-H. Sunwoo, S. Baik, O. K. Park, S. H. Choi, T. Hyeon, J. H. Kim, S. Lee and D.-H. Kim, *Sci. Adv.*, 2021, **7**, eabd3716.
14 C. Wang, X. Chen, L. Wang, M. Makihata, H.-C. Liu, T. Zhou and X. Zhao, *Science*, 2022, **377**, 517–523.

15 H. Wu, V. Sariola, C. Zhu, J. Zhao, M. Sitti and C. J. Bettinger, *Adv. Mater.*, 2015, **27**, 3398–3404.
16 S. Moreno, J. Keshtkar, R. A. Rodriguez-Davila, A. Bazaid, H. Ibrahim, B. J. Rodriguez, M. A. Quevedo-Lopez and M. Minary-Jolandan, *Adv. Electron. Mater.*, 2020, **6**, 2000391.
17 J. Goding, C. Vallejo-Giraldo, O. Syed and R. Green, *J. Mater. Chem. B*, 2019, **7**, 1625–1636.
18 X. Ren, M. Yang, T. Yang, C. Xu, Y. Ye, X. Wu, X. Zheng, B. Wang, Y. Wan and Z. Luo, *ACS Appl. Mater. Interfaces*, 2021, **13**, 25374–25382.
19 B. Lu, H. Yuk, S. Lin, N. Jian, K. Qu, J. Xu and X. Zhao, *Nat. Commun.*, 2019, **10**, 1043.
20 S. Zhang, Y. Chen, H. Liu, Z. Wang, H. Ling, C. Wang, J. Ni, B. Çelebi-Saltik, X. Wang, X. Meng, H. Kim, A. Baidya, S. Ahadian, N. Ashammakhi, M. R. Dokmeci, J. Travas-Sejdic and A. Khademhosseini, *Adv. Mater.*, 2020, **32**, 1904752.
21 H. Fan and J. P. Gong, *Macromolecules*, 2020, **53**, 2769–2782.
22 Y. Lee, W. J. Song and J.-Y. Sun, *Mater. Today Phys.*, 2020, **15**, 100258.
23 X. Liu, J. Liu, S. Lin and X. Zhao, *Mater. Today*, 2020, **36**, 102–124.
24 X. Chen, H. Yuk, J. Wu, C. S. Nabzdyk and X. Zhao, *Proc. Natl. Acad. Sci. U. S. A.*, 2020, **117**, 15497–15503.
25 J. Chen, H. Wen, G. Zhang, F. Lei, Q. Feng, Y. Liu, X. Cao and H. Dong, *ACS Appl. Mater. Interfaces*, 2020, **12**, 7565–7574.
26 R. An, X. Zhang, L. Han, X. Wang, Y. Zhang, L. Shi and R. Ran, *Mater. Sci. Eng., C*, 2020, **107**, 110310.
27 Z. Wang, J. Chen, Y. Cong, H. Zhang, T. Xu, L. Nie and J. Fu, *Chem. Mater.*, 2018, **30**, 8062–8069.
28 D. Zhang, Y. Tang, Y. Zhang, F. Yang, Y. Liu, X. Wang, J. Yang, X. Gong and J. Zheng, *J. Mater. Chem. A*, 2020, **8**, 20474–20485.
29 X. Pei, H. Zhang, Y. Zhou, L. Zhou and J. Fu, *Mater. Horiz.*, 2020, **7**, 1872–1882.
30 A. Yamamoto, H. Nakamoto, Y. Bessho, Y. Watanabe, Y. Oki, K. Ono, Y. Fujimoto, T. Terada and A. Ishikawa, *Med. Biol. Eng. Comput.*, 2019, **57**, 2741–2756.
31 Y. Dobashi, D. Yao, Y. Petel, T. N. Nguyen, M. S. Sarwar, Y. Thabet, C. L. W. Ng, E. Scabeni Glitz, G. T. M. Nguyen, C. Plesse, F. Vidal, C. A. Michal and J. D. W. Madden, *Science*, 2022, **376**, 502–507.
32 I. You, D. G. Mackanic, N. Matsuhisa, J. Kang, J. Kwon, L. Beker, J. Mun, W. Suh, T. Y. Kim, J. B.-H. Tok, Z. Bao and U. Jeong, *Science*, 2020, **370**, 961–965.
33 Y. M. Kim and H. C. Moon, *Adv. Funct. Mater.*, 2020, **30**, 1907290.
34 Q. Li, J. Li, D. Tran, C. Luo, Y. Gao, C. Yu and F. Xuan, *J. Mater. Chem. C*, 2017, **5**, 11092–11099.
35 S. Wang, K. Chen, M. Wang, H. Li, G. Chen, J. Liu, L. Xu, Y. Jian, C. Meng, X. Zheng, S. Liu, C. Yin, Z. Wang, P. Du, S. Qu and C. W. Leung, *J. Mater. Chem. C*, 2018, **6**, 4737–4745.
36 H. Kim, Y.-S. Kim, M. Mahmood, S. Kwon, N. Zavanelli, H. S. Kim, Y. S. Rim, F. Epps and W.-H. Yeo, *Adv. Sci.*, 2020, **7**, 2000810.
37 D. Lu, Y. Yan, R. Avila, I. Kandela, I. Stepien, M. Seo, W. Bai, Q. Yang, C. Li, C. R. Haney, E. A. Waters, M. R. MacEwan, Y. Huang, W. Z. Ray and J. A. Rogers, *Adv. Healthcare Mater.*, 2020, **9**, 2000942.
38 D. Lou, Q. Pang, X. Pei, S. Dong, S. Li, W. Tan and L. Ma, *Biosens. Bioelectron.*, 2020, **162**, 112275.
39 S. Choi, S. I. Han, D. Jung, H. J. Hwang, C. Lim, S. Bae, O. K. Park, C. M. Tschabrunn, M. Lee, S. Y. Bae, J. W. Yu, J. H. Ryu, S.-W. Lee, K. Park, P. M. Kang, W. B. Lee, R. Nezafat, T. Hyeon and D.-H. Kim, *Nat. Nanotechnol.*, 2018, **13**, 1048–1056.
40 Y. Ahn, H. Lee, D. Lee and Y. Lee, *ACS Appl. Mater. Interfaces*, 2014, **6**, 18401–18407.
41 J. Deng, H. Yuk, J. Wu, C. E. Varela, X. Chen, E. T. Roche, C. F. Guo and X. Zhao, *Nat. Mater.*, 2021, **20**, 229–236.
42 L. Han, X. Lu, M. Wang, D. Gan, W. Deng, K. Wang, L. Fang, K. Liu, C. W. Chan, Y. Tang, L.-T. Weng and H. Yuan, *Small*, 2017, **13**, 1601916.
43 J. W. Salatino, K. A. Ludwig, T. D. Y. Kozai and E. K. Purcell, *Nat. Biomed. Eng.*, 2017, **1**, 862–877.
44 N. Noskovicova, R. Schuster, S. van Putten, M. Ezzo, A. Koehler, S. Boo, N. M. Coelho, D. Griggs, P. Ruminski, C. A. McCulloch and B. Hinz, *Nat. Biomed. Eng.*, 2021, 1–20.
45 H. Yuk, B. Lu, S. Lin, K. Qu, J. Xu, J. Luo and X. Zhao, *Nat. Commun.*, 2020, **11**, 1604.
46 J. Wang, Q. Li, K. Li, X. Sun, Y. Wang, T. Zhuang, J. Yan and H. Wang, *Adv. Mater.*, 2022, **34**, 2109904.
47 M. Jia and M. Rolandi, *Adv. Healthcare Mater.*, 2020, **9**, 1901372.
48 H. Dechiraju, M. Jia, L. Luo and M. Rolandi, *Adv. Sustainable Syst.*, 2022, **6**, 2100173.
49 M. Guo, X. Yang, J. Yan, Z. An, L. Wang, Y. Wu, C. Zhao, D. Xiang, H. Li, Z. Li and H. Zhou, *J. Mater. Chem. A*, 2022, **10**, 16095–16105.
50 Y. Ohm, C. Pan, M. J. Ford, X. Huang, J. Liao and C. Majidi, *Nat. Electron.*, 2021, **4**, 185–192.
51 H. S. Song, O. S. Kwon, J.-H. Kim, J. Conde and N. Artzi, *Biosens. Bioelectron.*, 2017, **89**, 187–200.
52 Y. Zhang, M. Gong and P. Wan, *Matter*, 2021, **4**, 2655–2658.
53 M. Amjadi, K.-U. Kyung, I. Park and M. Sitti, *Adv. Funct. Mater.*, 2016, **26**, 1678–1698.
54 C. Boehler, S. Carli, L. Fadiga, T. Stieglitz and M. Asplund, *Nat. Protoc.*, 2020, **15**, 3557–3578.
55 H. Wei, D. Kong, T. Li, Q. Xue, S. Wang, D. Cui, Y. Huang, L. Wang, S. Hu, T. Wan and G. Yang, *ACS Sens.*, 2021, **6**, 2938–2951.
56 Z. Wang, Y. Liu, D. Zhang, K. Zhang, C. Gao and Y. Wu, *Compos. Sci. Technol.*, 2021, **216**, 109042.
57 Z. Wang, Y. Cong and J. Fu, *J. Mater. Chem. B*, 2020, **8**, 3437–3459.
58 X. Yu, W. Qin, X. Li, Y. Wang, C. Gu, J. Chen and S. Yin, *J. Mater. Chem. A*, 2022, **10**, 15000–15011.
59 A. M. El Badawy, R. G. Silva, B. Morris, K. G. Scheckel, M. T. Suidan and T. M. Tolaymat, *Environ. Sci. Technol.*, 2011, **45**, 283–287.
60 T. Mironava, M. Hadjiargyrou, M. Simon, V. Jurukovski and M. H. Rafailovich, *Nanotoxicology*, 2010, **4**, 120–137.

61 P. Mazurek, S. Vudayagiri and A. Ladegaard Skov, *Chem. Soc. Rev.*, 2019, **48**, 1448–1464.
62 K. Parida, J. Xiong, X. Zhou and P. S. Lee, *Nano Energy*, 2019, **59**, 237–257.
63 L. Jin, A. Chortos, F. Lian, E. Pop, C. Linder, Z. Bao and W. Cai, *Proc. Natl. Acad. Sci. U. S. A.*, 2018, **115**, 1986–1991.
64 X.-Y. Yin, Y. Zhang, X. Cai, Q. Guo, J. Yang and Z. Lin Wang, *Mater. Horiz.*, 2019, **6**, 767–780.
65 H. W. Kim, E. Kim, J. Oh, H. Lee and U. Jeong, *Adv. Sci.*, 2022, **9**, 2200687.
66 S. Cheng, Y. S. Narang, C. Yang, Z. Suo and R. D. Howe, *Adv. Mater. Interfaces*, 2019, **6**, 1900985.
67 C. Keplinger, J.-Y. Sun, C. C. Foo, P. Rothemund, G. M. Whitesides and Z. Suo, *Science*, 2013, **341**, 984–987.
68 Y. Zhu, C. Chao, C.-H. Cheng and W. W.-F. Leung, *IEEE Electron Device Lett.*, 2009, **30**, 337–339.
69 S. Wang, J. Zhang, O. Gharbi, V. Vivier, M. Gao and M. E. Orazem, *Nat. Rev. Methods Primers*, 2021, **1**, 1–21.
70 S. E. Feicht and A. S. Khair, *Soft Matter*, 2016, **12**, 7028–7037.
71 B. A. Yezer, A. S. Khair, P. J. Sides and D. C. Prieve, *J. Colloid Interface Sci.*, 2015, **449**, 2–12.
72 J. R. Macdonald and D. R. Franceschetti, *J. Chem. Phys.*, 1978, **68**, 1614–1637.
73 E. K. Lenzi, L. R. Evangelista, L. Taghizadeh, D. Pasterk, R. S. Zola, T. Sandev, C. Heitzinger and I. Petreska, *J. Phys. Chem. B*, 2019, **123**, 7885–7892.
74 J. R. Macdonald, L. R. Evangelista, E. K. Lenzi and G. Barbero, *J. Phys. Chem. C*, 2011, **115**, 7648–7655.
75 F. Ciucci, *Curr. Opin. Electrochem.*, 2019, **13**, 132–139.